Supplementary Information

Crystal structure response of corundum-type structures (α-Al_2O_3 and α-Fe_2O_3) under dynamic acoustic shocked conditions and comparison between static high-temperature and high-pressure conditions – Implications on volume-pressure-related phase transition types

Sivakumar Aswathappa[1], Lidong Dai[1*], Sahaya Jude Dhas Sathiyadhas[2], Raju Suresh Kumar[3], Haiying Hu[1*], Bing Lv[1], Xuefei Liu[1], Ziqiang Xu[1] Muthuvel Vijayan[4] and Rita Arul[5] and Abdulrahman I.Almansour[3]

[1]School of Physics and Electronic Science, Guizhou Normal University, Guiyang, 550025, China

[2]Saveetha School of Engineering, Saveetha Institute of Medical and Technical Sciences, Saveetha University, Chennai, Tamil Nadu, 602105, India

[3]Department of Chemistry, College of Science, King Saud University, P.O. Box 2455, Riyadh 11451, Saudi Arabia.

[4]Department of Physics, School of Foundation Science, Kumaraguru College of Technology, Coimbatore, Tamilnadu, 641 049, India

[5]Department of Physics, St. Anne's Degree College of Women, Halasuru, Bangalore – 560 008, Karnataka, India

Corresponding authors: dailidong@gznu.edu.cn and huhaiying@gznu.edu.cn

Experimental section

Shock wave loading procedure

The required shock waves are generated by an in-house semiautomatic Reddy Tube which is capable of producing shock waves. It has three sections such as driver, driven and diaphragm sections. The driver and driven sections are made of seamless steel tubes of length 48 cm and 33 cm, respectively and both have the same inner diameter of 1.5 cm. Atmospheric air is used as the working substance for the required shock wave generation which is supplied by a tabletop mini 1 HP air compressor that has the capacity of 8 bars pressure storage. The diaphragm section separates the driver section and the driven section. Carbonless paper diaphragms are fed into the diaphragm section with the help of a motor. While the atmospheric air is being compressed into the driver section, at the critical pressure, the diaphragm is ruptured such that the shock wave is generated and moves along the driven section.

An indigenously developed semi-automatic Reddy tube has been used to generate the shock waves. In the present experiment, shock waves of Mach number 2.2 have been utilized possessing the dynamic transient pressure of 2 MPa and temperature 864 K. The shock waves from the driven section go on striking the sample which is located 1 cm away from the open end of the driven section. One end of the driver section is connected to the diaphragm section which has two pneumatic cylinders and the other end is connected to the compressor. The pressurized air is also utilized for the operation of pneumatic cylinders. Using the pressure controller of the driver section, we can control the input pressure range of the driver section and the schamtic diagram is presented in **Fig. S1 (a, b).**

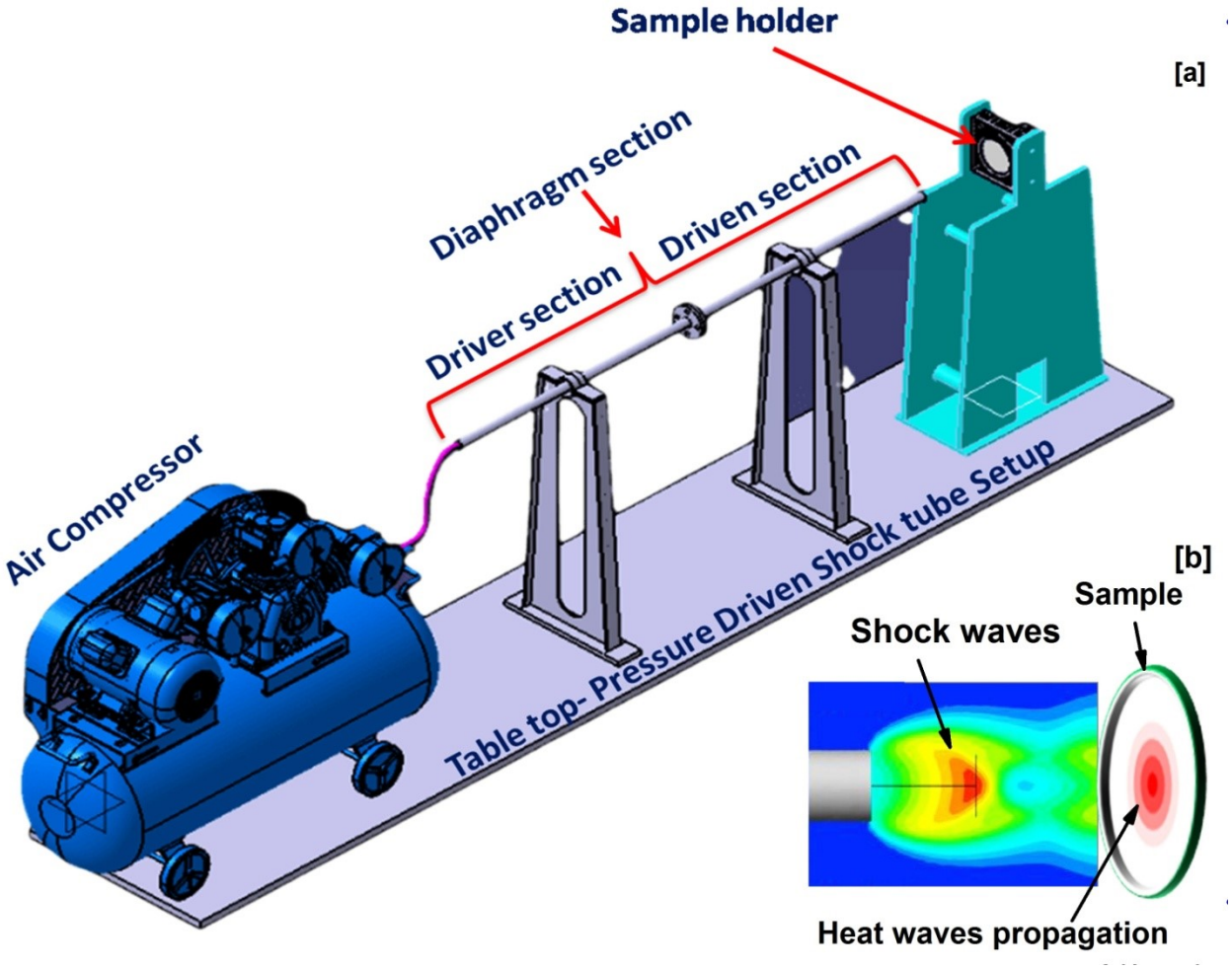

Fig. S1 (a) Schematic diagram of the table top pressure driven shock tube (b) shock propagation on the sample

Operation of the shock tube

Pressure of the air in the driver section is gradually increased by the air compressor until the diaphragm ruptures which leads to the generation of shock wave traveling along the axis of the driven section. The required numbers of test samples are to be placed one by one in the sample holder which is typically placed 1cm away from the open end of the driven section. Subsequently, required numbers of shock pulses are loaded on the respective test sample with an interval of 5 sec between each shock pulse. 100 number of shock pulse means that the sample is

exposed for 100 times by shock wave of a particular Mach number. After the completion of the shock wave loading experiment, the control and shock wave loaded samples are sent for analytical studies.

R-H relations

$$P2 = P1\left[1 + \frac{2\gamma}{\gamma+1}(M^2 - 1)\right] (1)$$

$$\frac{T_2}{T_1} = \frac{P_2}{P_1}\left[\frac{\left(\frac{\gamma+1}{\gamma-1}\right) + \frac{P_2}{P_1}}{1 + \left(\frac{\gamma+1}{\gamma-1}\right)\frac{P_2}{P_1}}\right] \quad (2)$$

$$\frac{P_5}{P_2} = \frac{(3\gamma-1)\frac{P_2}{P_1} - (\gamma-1)}{(\gamma-1)\frac{P_2}{P_1} + (\gamma+1)} (3)$$

$$\frac{T_5}{T_2} = \frac{P_5}{P_2}\left[\frac{\left(\frac{\gamma+1}{\gamma-1}\right) + \frac{P_5}{P_2}}{1 + \left(\frac{\gamma+1}{\gamma-1}\right)\frac{P_5}{P_2}}\right] (4)$$

The initial fixed values are P_1=1 bar, γ=1.4 and T=300 K, where M- Mach number, P_5 and T_5 stand for the reflected transient pressure and temperature at the end of the driven tube, respectively.

Analytical experiments

Powder X-ray diffraction

The analysis of Powder X-ray diffraction (PXRD) [Rigaku – Smart Lab X-Ray Diffractometer, Japan- CuKα1 as the X-ray source (λ = 1.5407 Å), with the step precision of ± 0.001°] was performed over the diffraction angle from 10-90 degree. The high-power X-ray is 9 kW and focus type is line focus. Active area is 384 mm^2 (19.2×20 mm). Spatial resolution is 75 μm and Global count rate is 2.5×10^8 (1×10^6 cps/pixel). Efficiency of this technique with target material of Cu is 99 %. Highest flux X-ray source: PhotonMax, HyPix-3000 high energy resolution 2D detector, New CBO family, with fully automated beam switchable CBO-Auto and Various operando measurements with the new SmartLab Studio II.

Field Emission Scanning Electron microscope

Field Emission Scanning Electron Microscope was used with (Carl Zeiss- Sigma 300), Resolution: 1.0 nm @ 15 kV, 1.6 nm @1kV Acceleration voltage: 0.02 kV to 30 kV. Magnification level was up to 10 lakhs times Smart EDX EDS analysis system and Probe current: 3 pA – 20 nA. 5-axes motorized eccentric specimen stage (X, Y=130 mm, Z=50 mm, T=-3°-70°, R-360°) and it offers a superior low kV performance approaching 1.5 nm at 1 kV. Digital store with maximum resolution of 32768 x 24576 Pixel was utilized. Windows 10 (64 bit) has been used to understand the surface morphology of the control and shocked Al_2O_3 and Fe_2O_3 NPs.

Ultra-Violet Diffused Reflectance spectroscopy

Ultra-violet Diffused Reflectance spectrometry (SHIMADZU UV 2600i) was utilized to record the optical properties of the Al_2O_3 and Fe_2O_3 NPs between 200 and 800 nm. The UV-2600i is equipped with Double-beam and Single monochromator to achieve ultra-low stray light levels that ensure constant optical resolution of 0.1 nm. The compact UV-2600i is a mid-range UV spectrophotometer that can be used in a wide array of fields, and easily expanded to suit your analysis goals. The included Shimadzu LabSolutions UV-Vis software is simple to use and can ensure data integrity. The UV-2600i is a single monochromator system, whose wavelength range can easily be expanded to the near-infrared region of 1400 nm using the optional integrating sphere. The UV- It is optimal for measuring samples with low transmittance. The UV-2600i is also equipped with Shimadzu's proprietary Lo-Ray-Ligh grade diffraction grating, which achieves high efficiency and low stray light levels. In addition, the UV-2600i achieves a significant noise reduction, and can accommodate measurements of solar cell anti-reflective films and polycrystalline silicon wafers.

Results and Discussion

Table. S1 Structural parameters of the control and shocked α-Al_2O_3 NPs

Parameters	Control	50 shocks	100 shocks	150 shocks	200 shocks
a **(Å)**	4.7608 (±0.0001)	4.7612 (±0.0001)	4.7609 (±0.0002)	4.7599 (±0.0001)	4.7598 (±0.0001)
b **(Å)**	4.7608 (±0.0001)	4.7612 (±0.0001)	4.7609 (±0.0002)	4.7599 (±0.0001)	4.7598 (±0.0001)
c (Å)	12.9963 (±0.0007)	12.9974 (±0.0008)	12.9968 (±0.0006)	12.9968 (±0.0008)	12.9962 (±0.0008)
α **(°)**	90	90	90	90	90
β **(°)**	90	90	90	90	90
γ **(°)**	120	120	120	120	120
Volume (Å^3)	255.1031 (±0.0010)	255.1650 (±0.0010)	255.1245 (±0.0010)	255.8990 (±0.0011)	255.8989 (±0.0010)
χ^2	1.91	2.51	2.37	1.83	2.29
GOF	1.4	1.6	1.5	1.3	1.4
Space group	*R*-3c	*R*-3c	*R*-3c	*R*-3c	*R*-3c

Table. S2 Structural parameters of the control and shocked α-Fe_2O_3 NPs

Parameters	Control	50 shocks	100 shocks	150 shocks	200 shocks
a **(Å)**	5.0179 (±0.0001)	5.0306 (±0.0001)	5.0299 (±0.0001)	5.0383 (±0.0002)	8.4078 (±0.0003)
b **(Å)**	5.0179 (±0.0001)	5.0306 (±0.0001)	5.0299 (±0.0001)	5. 0383 (±0.0002)	8.4078 (±0.0003)
c (Å)	13.7346 (±0.0007)	13.7346 (±0.0007)	13.7621 (±0.0006)	13.7803 (±0.0008)	8.4078 (±0.0003)
α **(°)**	90	90	90	90	90
β **(°)**	90	90	90	90	90
γ **(°)**	120	120	120	120	90
Volume ($Å^3$)	299.7127 (±0.0011)	310.7683 (±0.0012)	301.5579 (±0.0011)	255.8990 (±0.0011)	594.3505 (±0.0012)
χ^2	5.33	3.94	2.37	1.41	1.05
GOF	2.3	2.1	1.5	1.2	1.2
Space group	(*R*-3c)	*R*-3c	*R*-3c	*R*-3c	Fe_3O_4 (Fd-3m)

α-Fe_2O_3 to Fe_3O_4 conversion mechanism

The hematite NPs exhibit a diffraction peak at 30.34° that may belong to Fe_3O_4 NPs which might have been generated during the annealing process at 700°C. The intensity of the characteristic peak of the (110) plane is substantially reduced corresponding to the number of shock pulses i.e., 50, 100 and 150 shocked conditions. Moreover, the (110) plane is found to have continually shifted towards the lower diffraction angle according to the number of shock pulses and the observed lower-angle shift provides the key indication of enhancement of cell volume of the hematite and increase in the Fe-O bond length with respect to the number of shock pulses. However, it could be noted that, up to 150 shocked conditions, there is neither crystallographic nor molecular phase change observed as in the previous work. The observed XRD pattern of the control hematite NPs at 200 shocked conditions is presented in Fig.7b. Surprisingly, a complete conversion is observed, i.e., from the hematite to the magnetite (Fe_3O_4) and the obtained XRD pattern is well-matched with the standard XRD pattern of the magnetite [**1**]. In the present case, the required minimum energy for the phase transition from α-Fe_2O_3 to Fe_3O_4 might have been supplied by the applied shock pulses inducing the breakage of the Fe-O bonds in the atomic structure which could have resulted into the local volume collapse and high temperature induced reduction process in hematite enforcing dynamic re-crystallization.

It could be noted that, for the test sample, the bond nature and the total number of coordination bonds have not changed up to 150 shocked conditions. However, the bond length of Fe-O might have increased whereas the bond strength has reduced such that the system is on the

verge of jumping to the next available crystallographic phase due to the impact of shock waves while increasing the number of shock pulses. At the same time, it reaches the minimum energy barrier of the thermodynamic system of α-Fe_2O_3 so that the unit cell volume may increase subsequently with respect to the number of shock pulses. Note that α-Fe_2O_3 and Fe_3O_4 have the unit cell volume of 301 $Å^3$(JCPDS 24-0072**)** and 591 $Å^3$ **(**JCPDS 11-0614**)**, respectively almost with the ratio 1:2. The test crystal structure could not sustain its original crystallographic phase during the shock-wave-loaded condition because of the existing high-transient pressure and temperature. Hence, the weakest surface Fe-O bonds may break first and try to re-organize for the next available crystal structure. In addition to that, the large C-axis length of the hematite (bond length = 13.7471 Å) is highly favorable for such bond breakages enforced by shock waves and while increasing the number of shocks, the ratio of c/a may increases, which attributes to either a bonding distortion or an uneven modification of Fe-O-Fe bond lengths. The observed phase-transitions of α-Fe_2O_3 to Fe_3O_4 NPs is probably reconstructive and spin-type phase-transitions while not the decomposition of α-Fe_2O_3. Due to the significant super heating effect, Fe_3O_4 has formed rather the high pressure phase of the corundum α-Fe_2O_3. α-Fe_2O_3 has only Fe^{3+} ions whereas Fe_3O_4 has mixed ions such as Fe^{3+} and Fe^{2+}. The possible explanation of the observed shock wave induced spin transition of α-Fe_2O_3 to Fe_3O_4 is that, for a particular octahedron, the Fe–O bond lengths and the octahedral volume increase gradually with the increase of the number of shock pulses. Moreover, at a certain point in the pressure scale, the minimum Fe–O bond length in that particular octahedron reaches a value for which the octahedral crystal field dominates over the exchange energy such that the particular octahedron acquires a new spin state switching from its $3t_{2g}\, e_g^2$ (high spin configuration) state to $5t_{2g}\, 0e_g$ (low spin configuration), resulting in the collapse of the octahedral volume. The applied shock waves

might have induced the oxygen vacancies based on the Fe and O systems. Since α-Fe_2O_3 is an oxygen-rich system compared to Fe_3O_4, there are many possibilities for initiating the reduction process at high-temperature and high-pressure conditions resulting in the observed oxygen poor system in Fe and O system rather than the polymorphic phases and the similar kind of results have been observed at high power laser irradiation conditions [2].

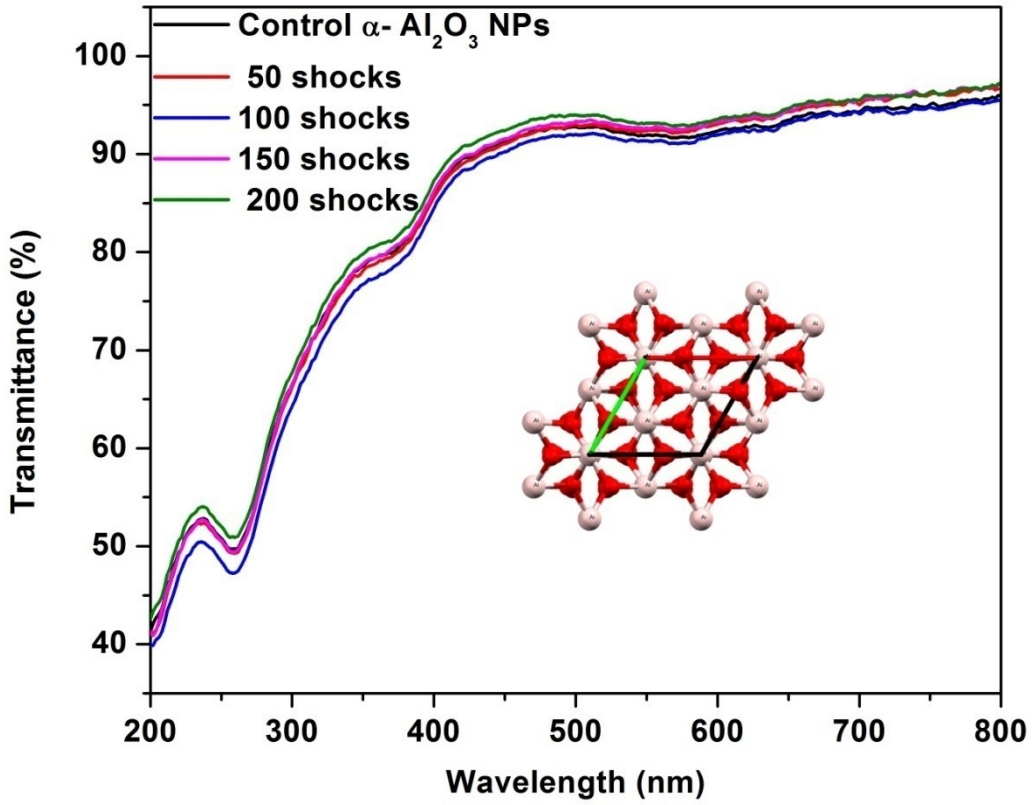

Fig. S2 Optical transmittance spectra of the control and shocked $A_{l2}O_3$ NPs

References

[1] S. Liu, K. Yao, L. H. Fu and M. G. Ma, Selective synthesis of Fe_3O_4, ϒ-Fe_2O_3, and α-Fe_2O_3 using cellulose-based composites as precursors. RSC Adv. 6, 2135 (2016)

[2] N. M. Ferreira, M. C. Ferro, G. Gaspar, A. J. S. Fernandes, M. A. Valente and F. M. Costa, Laser-induced hematite/magnetite phase transformation. J. Elect. Mater 49, 7187–7193 (2020).